Available online at www.sciencedirect.com
ScienceDirect
Journal of Power Sources 173 (2007) 599–605
JOURNAL OF POWER SOURCES
www.elsevier.com/locate/jpowsour

Solid state synthesis of hydrous ruthenium oxide for supercapacitors

Yan-Yu Liang [a], Hu Lin Li [a,b], Xiao-Gang Zhang [a,*]

[a] College of Materials Science and Technology of Nanjing University of Aeronautics and Astronautics, Nanjing 210016, PR China
[b] College of Chemistry and Chemical Engineering of Lanzhou University, Lanzhou 730000, PR China

Received 9 February 2007; received in revised form 2 August 2007; accepted 8 August 2007
Available online 10 August 2007

Abstract

A novel solid state route has been successfully developed for the synthesis of nano-scale hydrous ruthenium oxide (denoted as $RuO_2{\cdot}xH_2O$). The procedure involves directly mixing $RuCl_2{\cdot}xH_2O$ with alkali to form $RuO_2{\cdot}xH_2O$ in a mortar at room temperature. Transmission electron microscopy (TEM) and N_2 adsorption–desorption measurement indicate that the $RuO_2{\cdot}xH_2O$ particle is approximately 30–40 nm with mesoporous structure. The crystalline structure and the electrochemical properties of $RuO_2{\cdot}xH_2O$ have been systematically explored as a function of annealing temperature. At lower temperatures, the $RuO_2{\cdot}xH_2O$ powder was found in an amorphous phase and the maximum capacitance of 655 F g^{-1} was obtained by annealing at 150 °C. Higher temperatures (exceeding 175 °C) presumably converted amorphous phase into crystalline one and the corresponding specific capacitance dropped rapidly from 547 F g^{-1} at 175 °C to 87 F g^{-1} at 400 °C. Also, the dependence of electrochemical performance on annealing conditions of $RuO_2{\cdot}xH_2O$ was investigated by electrical impedance spectroscopy (EIS) study.

Keywords: Solid state reaction; Hydrous ruthenium oxide; Capacitive performance; Electrochemical capacitors; Electrical impedance spectroscopy

1. Introduction

Growing environmental concerns and increasing depletion of fossil fuels have created interest in alternative energy technologies. Electrochemical redox capacitors (supercapacitors) are widely recognized as promising devices exhibiting much higher capacity and higher power characteristics in comparison with conventional dielectric capacitors and rechargeable batteries systems, respectively. The high capacity of supercapacitors mainly comes from the faradic reaction within electroactive materials (i.e., pseudocapacitance) [1–4], or the high specific surface area of electrode materials (i.e., double layer capacitance) [3–5]. The high power performance of supercapacitors is attributed to the fast charge–discharge characteristics of a double layer process or the high electrochemical reversibility of redox transitions within electrode materials [6]. Thus, supercapacitors are becoming attractive energy storage systems particularly for applications involving high power requirements. For example, hybrid systems consisting of batteries and supercapacitors are being pursued for electric vehicle propulsion. In such hybrid systems, supercapacitors can provide the peak power during acceleration and therefore the batteries can be optimized primarily for higher energy density and better cycle life.

Among the electroactive materials, RuO_2 has been recognized as the most promising candidate due to its advantages of a wide potential window, highly reversible redox reaction [7], remarkably high specific capacitance [8] and excellent cycle life. Anhydrous RuO_2 is a d-band metallic conductor, with a single crystal conductivity of 10^4 S cm^{-1} [9]. Alternatively, the hydrous form of RuO_2, denoted as $RuO_2{\cdot}xH_2O$ or RuO_xH_y, is a mixed proton and electron conductor. In 1995, Zheng et al. [7,10] firstly prepared hydrous $RuO_2{\cdot}xH_2O$ by the sol–gel way with the novel specific capacitances as high as 720 F g^{-1}. As he reported, only amorphous $RuO_2{\cdot}xH_2O$ annealed at a critical temperature close to its crystalline temperature was found to possess the maximum specific capacitance value among all the samples. After this breakthrough, $RuO_2{\cdot}xH_2O$ was synthesized via various methods to meet the increasing demand for power storage systems, including cyclic voltammetric deposition [2], anodic deposition [11], spray deposition [12], hydrothermal synthesis [13], oxidative synthesis [6] and incipient wetness method [14]. However, to the best of our knowledge, special conditions, tedious procedures or complex apparatus may be required for these above methods. On the other hands, the low abundance

* Corresponding author. Tel.: +86 25 52112626; fax: +86 25 52112626.
E-mail address: azhangxg@nuaa.edu.cn (X.-G. Zhang).

0378-7753/$ – see front matter © 2007 Elsevier B.V. All rights reserved.
doi:10.1016/j.jpowsour.2007.08.010

and high cost of the precious metal are major limitations to commercial application [15]. With these considerations, how to achieve a simple, cost-effective procedure with a high product yield is very worth of being developed to resolve these issues.

Comparing with the other synthesis methods, solid state reaction has characteristic feature: it enables one to synthesize materials in one pot without the solvent pollution at room temperature [16,17]. Moreover, crystalline powders can be prepared by directly mechanical mixing of raw materials and the need for subsequent chemical treatment is eliminated. Recently, Xin and his colleagues [17–19] have proposed a simple solid state reaction for preparation of a series of nanocrystal oxides and sulfide. In their process, the precursors of metal oxide were obtained by directly mixing the corresponding metal salts and alkalis with or without surfactant in a mortar at room temperature.

The purpose of this work is to employ the solid state procedure to prepare $RuO_2{\cdot}xH_2O$, and taking it as the electrode materials for supercapacitors, directly from the common reagent sources of $RuCl_3{\cdot}xH_2O$ and NaOH. It has demonstrated the final product of $RuO_2{\cdot}xH_2O$ possessing relatively novel specific capacitance properties with more than 90% product yield. Simplicity, high yield, environmental friendliness and economic viability factors make $RuO_2{\cdot}xH_2O$ by this solid state synthesis technique very attractive.

2. Experimental

2.1. Synthesis of $RuO_2{\cdot}xH_2O$ nanoparticles

All the chemical reagents used in this experiment were analytical grade. The procedure employed for preparing $RuO_2{\cdot}xH_2O$ is as follows: in a typical synthesis, $RuCl_3{\cdot}xH_2O$ (2.07 g, about 0.01 mol) was ground for 5 min in an agate mortar at room temperature. Then, the dark gray powder was fully mixed with NaOH (0.44 g, 0.011 mol) to form the product of $RuO_2{\cdot}xH_2O$. After grinding for 30 min, it was stood for 2 h. The black material was washed several times using a centrifugal filtration method with distilled water and alcohol. Finally, the powder material, $RuO_2{\cdot}xH_2O$, was divided into six portions and heated from 100 °C to 400 °C in air for 3 h, respectively.

2.2. Material characterizations

The thermal behavior of $RuO_2{\cdot}xH_2O$ was obtained in air using a Perkin Elmer TG (PE7, USA) thermal analyzer at a heating rate of 10 °C min^{-1}. The crystal structures were identified by X-ray diffractometer (D8, BRUKER) using Cu Kα radiation. TEM (FEI Tecnai G^2 20 S-TWIN) and SEM (FEI, QUANTA-200) were employed to examine the morphology properties. The specific surface areas and mean pore sizes were obtained from a surface area analyzer (Micrometritics, ASAP 2010).

2.3. Electrode preparation

The working electrodes were prepared in term of the literature reported method [7]. 80 wt% of electroactive $RuO_2{\cdot}xH_2O$ powder was mixed with 7.5 wt% of acetylene black (>99.9%) and 7.5 wt% of conducting graphite in an agate mortar until a homogeneous black powder was obtained. To this mixture, 5 wt% of poly(tetrafuoroethylene) dried powder (PTFE) was added with a few drops of ethanol. After brief evaporation drying, the resulting paste was pressed at 5 MPa to stainless gauze with a stainless wire for electric connection. The electrode assembly was dried for 16 h at 70 °C in air. Each electrode contained 10 mg redox active material and has a geometric surface area of about 1 cm^2.

2.4. Electrochemical measurements

Electrochemical measurements were carried out using a CHI660 electrochemical working station (Chenhua, Shanghai) in a half-cell set up configuration at room temperature. A platinum gauze electrode and a saturated calomel electrode (SCE) served as the counter electrode and the reference electrode, respectively. Cyclic voltammogram was collected by polarizing the working electrode between 0 V and 1 V in 0.5 M H_2SO_4 aqueous solution. The galvanostatic charge–discharge of the electrodes was evaluated in the potential range from 0 V to 0.95 V. Impedance properties of the prepared electrodes were characterized by electrical impedance spectroscopy in open-circuit conditions and the data were collected in the frequency range of 10^5 Hz to 10^{-2} Hz.

3. Results and discussion

The TG and corresponding DTG analyses are illustrated in Fig. 1. From the TG curve, it is shown that the weight decreased continuously as the temperature was raised from room temperature to about 330 °C. Taking account of decomposition of RuO_2 to Ru metal does not occur at the temperature less than 1000 °C, the correlative weight loss is almost attributed to loss of bound water or crystalline phase transition. From the DTG curve, one wave-like and one peak were observed at the specific temperatures of below 200 °C and 330 °C, respectively. Combined with the TG results, it can be seen that the one wave-like below 200 °C is due to the vaporization of H_2O in the $RuO_2{\cdot}xH_2O$ system. The peak at 330 °C is accompanied with the crystalline

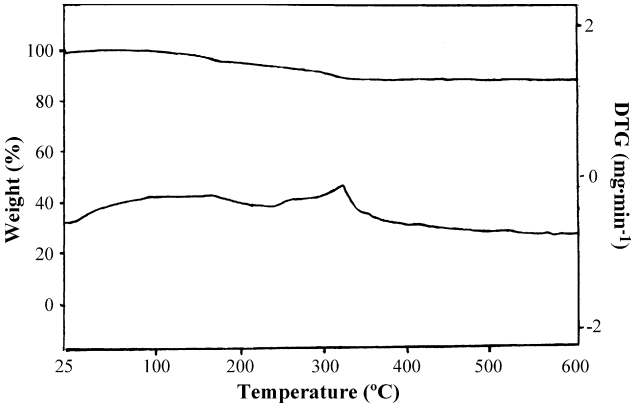

Fig. 1. TG and DTG data of the $RuO_2{\cdot}xH_2O$ precursor.

phase transition of ruthenium oxide, which is higher than the temperature where the crystalline phase was firstly detected by the XRD results discussed below. It can be reasonable, since the crystalline transition is dependent not only on the specific temperature but also on the amount of energy absorbed directly associated with the heating scan rate [7]. The difference found in the crystallization temperature by TG and XRD come from the fact that the thermal treatments done are different, while in the former technique, temperature was increased at 10 °C min^{-1}, in the latter one, each temperature was kept for 3 h. The percent change in weight from room temperature to 330 °C is totally about 12%, suggesting that the sample could be $Ru(OH)_3$ or $RuO_2{\cdot}H_2O$ (by oxidation in air), because their molecular weights are also the same or at least very close [7]. Increasing the annealing temperature simply dehydrated the $RuO_2{\cdot}H_2O$ to $RuO_2{\cdot}xH_2O$ ($0 \leq x \leq 1$). At the temperature above 330 °C, anhydrous RuO_2 was formed.

Fig. 2 displays SEM and TEM images of $RuO_2{\cdot}xH_2O$ annealed at 100 °C. As shown in Fig. 2a and b, the $RuO_2{\cdot}xH_2O$ powder has the morphology of round-like particles. The novel irregular particle morphology indirectly implies $RuO_2{\cdot}xH_2O$ has

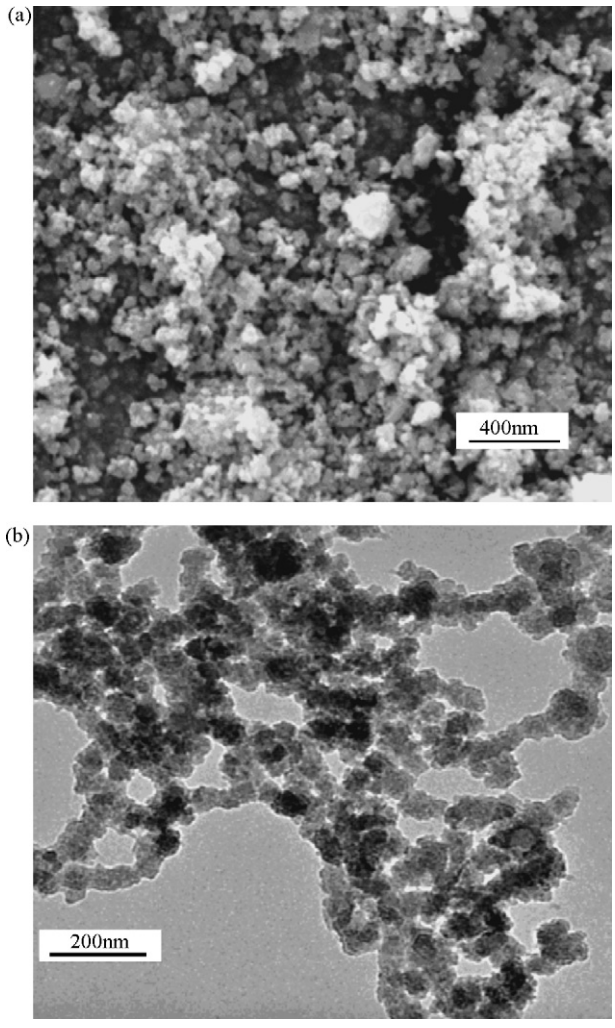

Fig. 2. (a) SEM image $RuO_2{\cdot}xH_2O$ annealed at 100 °C and (b) TEM image of $RuO_2{\cdot}xH_2O$ annealed at 100 °C.

Table 1
Textural properties of $RuO_2{\cdot}xH_2O$ samples from N_2 adsorption–desorption measurement

Sample	BET surface (m^2 g^{-1})	Pore volume (cm^3 g^{-1})	Pore size (nm)
RuO_2-100	78.5741	0.170557	8.6826
RuO_2-200	43.6409	0.170634	15.63981
RuO_2-300	40.1389	0.194722	19.40479

possessed a low crystalline structure. Typical particle diameter is about 30–40 nm with narrow size distribution. From the TEM image, it seems that $RuO_2{\cdot}xH_2O$ shows a mesoporous structure. This point could be confirmed by nitrogen adsorption–desorption isotherms (see Fig. 3). It is noteworthy that the unique porous morphology structure shows an anisotropic morphology characteristic, which allows a good access of electroactive ions diffusion and migration in the electrolyte to $RuO_2{\cdot}xH_2O$.

The N_2 adsorption–desorption measurements at liquid N_2 temperature was used to study mesoporosity and textural properties of $RuO_2{\cdot}xH_2O$ annealed at 100 °C, 200 °C and 300 °C, respectively. Fig. 3 depicts the N_2 adsorption–desorption isotherm and pore size distribution of the samples. It can be found that all the isotherms revealed a typical type IV sorption behavior, representing the mesoporous structure characteristic according to the classification of IUPAC [20]. As shown in the inset of Fig. 3, the pore size distribution from BJH method showed very narrow and monomodal in the mesopore region (2–50 nm), indicating the good quality properties of the $RuO_2{\cdot}xH_2O$ sample by this solid state synthesis. Also the textural properties of the three $RuO_2{\cdot}xH_2O$ samples are given in Table 1. As shown in table, the BET surface area of the sample annealed at 100 °C is 78.5741 m^2 g^{-1}, with mean pore diameter and pore volume is 8.6826 nm and 0.170557 cm^3 g^{-1}, respectively. When the samples are subjected to a higher heat-treatment temperature, the pore diameter and the pore volume abruptly increase. At the same time, the specific surface area decreases drastically. This can be explained, as the low-temperature sample possesses more complicated microtexture than the high-temperature ones.

The XRD pattern of the $RuO_2{\cdot}xH_2O$ sample annealed from 100 °C to 400 °C is shown in Fig. 4. At lower temperatures, the material is amorphous phase in nature and this is confirmed by the featureless diffraction peaks seen at 100 °C and 150 °C. When the temperature was raised to 175 °C, the XRD patterns have exhibited the characteristic peaks of anhydrous RuO_2 at 28.04°, 35.08° and 54.28°, respectively. Also, the peak intensities increase and the width decreases with further increasing the annealing temperature. The XRD data show that change in annealing temperature has significantly altered the crystalline nature of the samples.

Cyclic voltammogram (CV) of a half-cell in the potential range between 0 V and 1 V was employed to evaluate the electrochemical characteristics of $RuO_2{\cdot}xH_2O$. In Fig. 5, the CV curves of $RuO_2{\cdot}xH_2O$ annealed at 100 °C exhibit a rectangular shape. As increasing the scan rate, no obvious distortions in CV

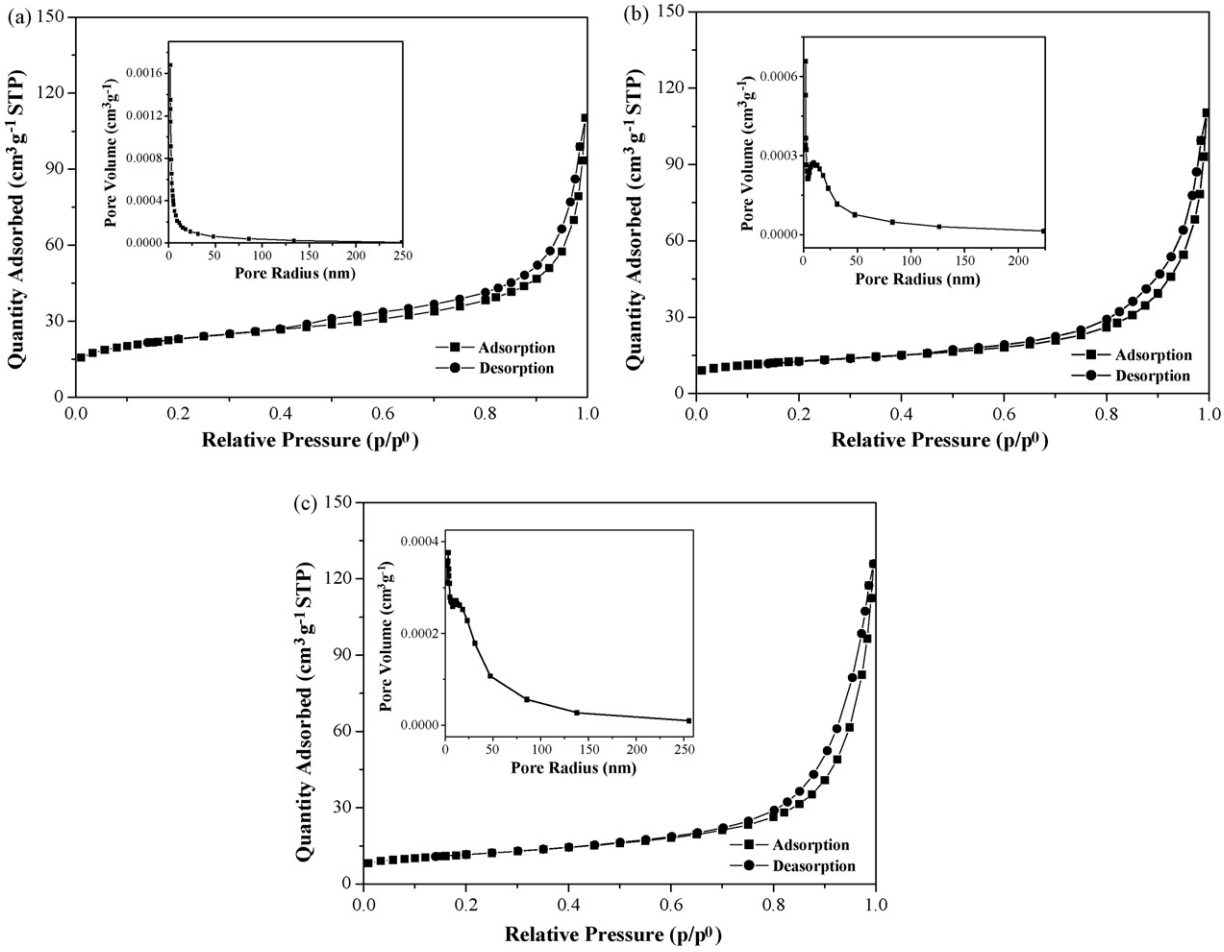

Fig. 3. N_2 adsorption–desorption isotherm and pore size distribution (inset) of (a) $RuO_2{\cdot}xH_2O$ annealed at 100 °C. (b) $RuO_2{\cdot}xH_2O$ annealed at 200 °C. (c)$RuO_2{\cdot}xH_2O$ annealed at 300 °C.

was observed and the ratio of anodic to cathodic charge (Q_a/Q_c) almost remains close to one in all cases. This result suggests the electrochemical process at the interface is highly reversible. Also the effect of annealing temperature on the electrochemical performance of $RuO_2{\cdot}xH_2O$ was systematically explored. Taking account of the similar CV behavior of $RuO_2{\cdot}xH_2O$ annealed at different temperatures, the corresponding CVs were not shown individually in this paper.

Fig. 6 presents the typical galvanostatic charge–discharge curves for $RuO_2{\cdot}xH_2O$ annealed at 150 °C under the applied current range from 1 mA cm^{-2} to 32 mA cm^{-2}. The pseudocapactive behavior of $RuO_2{\cdot}xH_2O$ is clearly observed from the

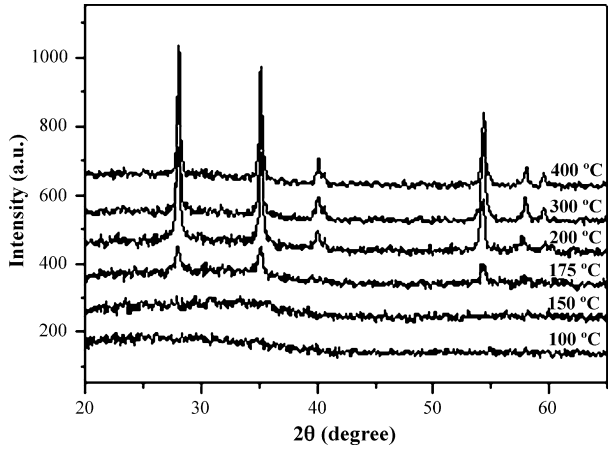

Fig. 4. XRD patterns of $RuO_2{\cdot}xH_2O$ annealed at different temperatures.

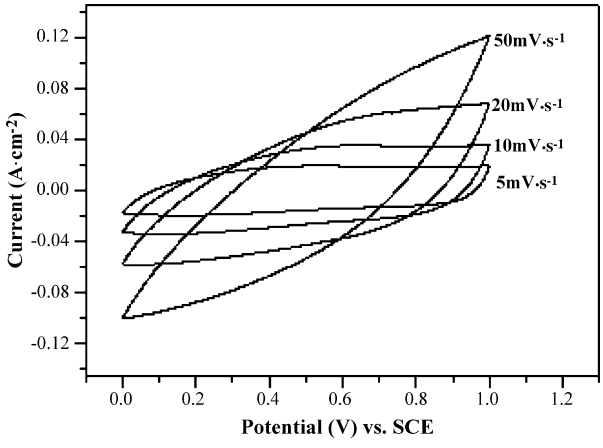

Fig. 5. Cyclic voltammograms of $RuO_2{\cdot}xH_2O$ annealed at 100 °C at different scan rates in 0.5 M H_2SO_4 within a potential window of 0–1 V.

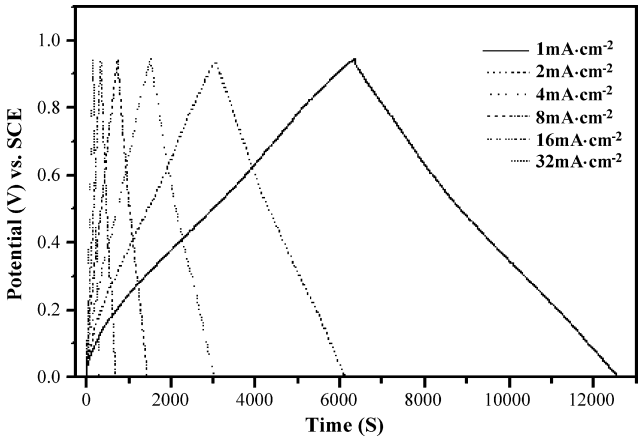

Fig. 6. Charge–discharge behavior of $RuO_2{\cdot}xH_2O$ annealed at 150 °C at different current densities in 0.5 M H_2SO_4 within a potential window of 0–0.95 V.

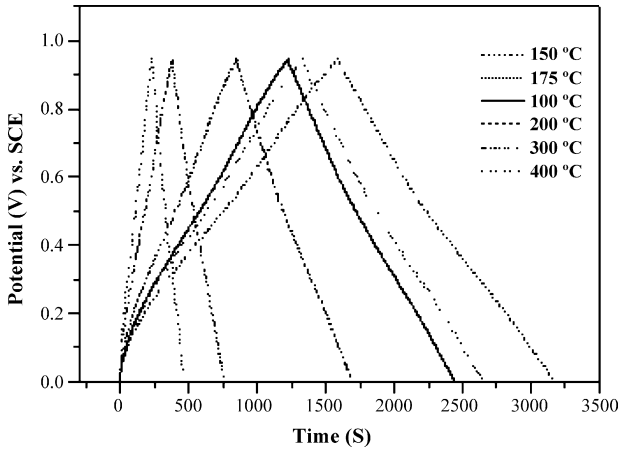

Fig. 7. Charge–discharge behavior of $RuO_2{\cdot}xH_2O$ annealed at different temperatures at the 4 mA cm^{-2} current density in 0.5 M H_2SO_4 within a potential window of 0–0.95 V.

departion from linearity of the *V–t* plots. The specific capacitance was determined using the following equation:

$$C = \frac{It}{m\Delta V} \quad (1)$$

where I is the specific discharge current, t the overall discharge time, ΔV the potential range and m is the mass of electroactive material. Based on Eq. (1), the $RuO_2{\cdot}xH_2O$ electrode discharged from 1 mA cm^{-2} to 32 mA cm^{-2} yields the specific capacitance is 655 F g^{-1}, 637 F g^{-1}, 626 F g^{-1}, 598 F g^{-1}, 556 F g^{-1}, 487 F g^{-1}, respectively. The better specific capacitance performance is mainly attributed to active ions intercalation into the bulk material of hydrous amorphous ruthenium oxides; not only on the surface of electrodes. The specific capacitance of $RuO_2{\cdot}xH_2O$ annealed at 150 °C is decreased from 655 F g^{-1} to 474 F g^{-1}, when the discharge current applied is changed from 1 mA cm^{-2} to 32 mA cm^{-2}. The loss in specific capacitance is about 26%, which has been reasonably assigned to the presence of inner active sites that could not accessed by the electroactive ions to proceed with the redox transition completely at higher current density, thereby causing a decline in specific capacitance [21].

Fig. 7 presents the galvanostatic charge–discharge curves of $RuO_2{\cdot}xH_2O$ annealed at the range from 100 to 400 °C at 4 mA cm^{-2}. It is distinct that the capacitance value increased initially with increasing the annealing temperature. The maximum value of 626 F g^{-1} was obtained at 150 °C. When the temperature ascended higher than 175 °C, it dropped significantly. At 200 °C, the value of 349 F g^{-1} and on heating to 300 °C, it evidently decreased to 122 F g^{-1}. Up to 400 °C, it only 87 F g^{-1}. According to Zheng et al. [7], the electrochemical reaction of $RuO_2{\cdot}xH_2O$ is similar to that of RuO_2, that means both of them can be oxidized and reduced reversibly through the electrochemical protonation.

$$RuO_2 + \delta H^+ + \delta e^- \leftrightarrow RuO_{2-\delta}(OH)_\delta,\ 0 \le \delta \le 2 \quad (2)$$

The change in capacitance characterization of $RuO_2{\cdot}xH_2O$ and RuO_2 has been attributed to the concept that an amorphous structure of $RuO_2{\cdot}xH_2O$ retains the facile pathways for electron and proton conduction, while crystalline RuO_2 decreases the proton transport rate.

Based on the charge storage mechanism mentioned above, the small sine wave amplitude of 5 mV and broad frequency range of 10^5 Hz to 10^{-2} Hz used for EIS. Fig. 8 shows the complex-plane plot of the impedance of the $RuO_2{\cdot}xH_2O$ annealed at a range from 150 °C to 400 °C, respectively. In the most high frequency region, R_Ω, is about from 1.6 Ω to 1.5 Ω. As the electrolyte resistance and the contact resistance are almost identical in all cases, a slightly decrease of R_Ω indicates a decrease of $RuO_2{\cdot}xH_2O$ electrode resistance itself. In the high frequency region, R_{ct} the resistance of charge transmission evidently decreases with increasing the annealing temperature, which goes from 0.9 Ω at 150 °C to 0.4 Ω at 400 °C. In fact, this is directly connected with pore structure of the interparticles [22–24], the lower annealing temperature is, the smaller particle diameter is, the more complicated the pore structure is, then the more difficult the transmission of charge is. However, the complicated pore structure is very helpful to increase the overall active sites (or the overall active area) for going along with the faradic

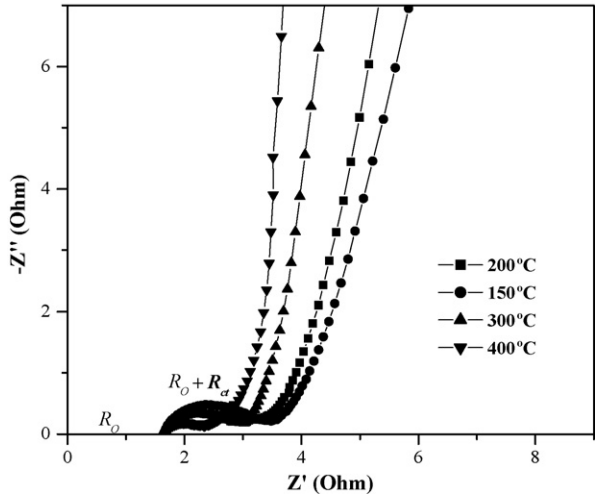

Fig. 8. The impedance plots of $RuO_2{\cdot}xH_2O$ annealed at different temperatures.

reactions in turn, leading to better capacitive performance of $RuO_2 \cdot xH_2O$ annealed at low temperature. In the low frequency region, $RuO_2 \cdot xH_2O$ annealing at 150 °C temperature shows a little more closer slope of 45° among all the temperatures, which implies that it is more strongly controlled by the diffusive activity. This may be correlated with the $RuO_2 \cdot xH_2O$ annealed at 150 °C provided with an amorphous crystalline structure shown in Fig. 4. When increasing the temperature, the integrated crystalline phase has occurred, increasing particle diameter and decreasing the distance for diffusion, enhanced the diffusive activity of electrolyte within the electrode material. Therefore, the diffusing regions, especially for annealing at 400 °C, come closer to an ideal straight line. On the whole, the higher annealing temperature is contributed to the smaller value of R_{ct}, but cannot compensate loss capacitance because of increasing particles diameter and result in the decreasing the effective active sites for faradic reactions taking place.

The specific capacitance of the capacitor at different annealed temperatures can be evaluated from impedance test according to the following equation:

$$C = \frac{1}{m \times j \times 2\pi f \times Z''} \quad (3)$$

where C is the specific capacitance; f the frequency; Z'' the imaginary parts of the impedance test and m is the mass of the active materials. By calculation, the specific capacitance at the temperature range from 150 °C to 400 °C is 518 F g^{-1}, 291 F g^{-1}, 112 F g^{-1}, 73 F g^{-1}, respectively. The data are smaller than those of the galvanostatic charge–discharge results, which are in accordance with Wang et al. report [25,26].

The stability of $RuO_2 \cdot xH_2O$ powder annealed at 150 °C was studied in the cycle number of 1000. Fig. 9 shows the corresponding capacitance value as a function numbers at a 4 mA cm^{-2}current. The specific capacitance decayed 5% during the first 100 cycles, and afterward it was much more stable and only decayed another 5% until the 1000th cycle. It is obvious that the loss of capacitance is little during the charge and discharge cycles. So $RuO_2 \cdot xH_2O$ prepared by the simple method can be considered as promising materials in the application of supercapacitors. The capacitance decay during the first 100 cycle is believed to be related to oxygen evolution; on account of the open potential of $RuO_2 \cdot xH_2O$ is close to the potential of oxygen evolution.

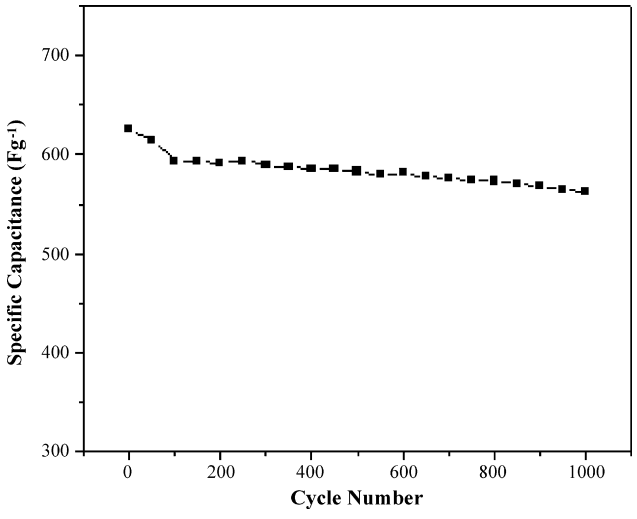

Fig. 9. Cycle life of the $RuO_2 \cdot xH_2O$ annealed at 150 °C at the current density of 4 mA cm^{-2}.

4. Conclusion

We have successfully developed a novel solid state synthetic route for the preparation of mesoporous hydrous ruthenium oxide. The primary efforts have been focused on exploring the relationships among the annealing conditions, structural changes and the electrochemical performances. Combined with the existing results, it was found that the specific capacitance of $RuO_2 \cdot xH_2O$ is strongly dependent on the corresponding crystalline structure. The high value of specific capacitance can be obtained only from the amorphous phase. Once the crystalline phase was formed, the specific capacitance dropped rapidly. For example, a maximum capacitance of 655 F g^{-1} was obtained by annealing at 150 °C (single electrode). Higher temperatures (exceeding 175 °C) presumably contributed amorphous phase of $RuO_2 \cdot xH_2O$ into crystalline one and the corresponding specific capacitance dropped rapidly from 547 F g^{-1} at 175 °C to 87 F g^{-1} at 400 °C. Although, it is not provided with the best electrochemical performance, in paralleling with the classical sol–gel method, this procedure is a simple, efficient and environmentally friendly method to synthesize $RuO_2 \cdot xH_2O$. In addition, the $RuO_2 \cdot xH_2O$ has highly stable behavior in the electrolyte after long term cycling. With these properties, the novel solid state synthesis is an excellent method for potentially useful ruthenium oxide.

Acknowledgements

This work was supported by the National Natural Science Foundation of China (Nos. 20403014; 20633040), the National Natural Science Foundation of Jiangsu Province (No. BK2006196), the Post-doctoral Science Foundation of China (No. 20060400283) and the Post-doctoral Science Foundation of Jiangsu Province (No. 2006277).

References

[1] S. Sarangapani, B.V. Tilak, C.P. Chem, J. Electrochem. Soc. 143 (1996) 3791.
[2] C.C. Hu, Y.H. Huang, J. Electrochem. Soc. 146 (1999) 2465.
[3] B.E. Conway, Electrochemical Supercapacitors, Kluwer–Plenum, New York, 1999.
[4] A. Burke, J. Power Sources 91 (2000) 37.
[5] Y.R. Nian, H. Teng, J. Electrochem. Soc. 149 (2002) A1008.
[6] K.H. Chang, C.C. Hu, J. Electrochem. Soc. 151 (2004) A958.
[7] J.P. Zheng, P.J. Cy Gan, T.R. Jow, J. Electrochem. Soc. 142 (1995) 2699.
[8] I. Liu, W.G. Pell, B.E. Conway, Electrochim. Acta 42 (1997) 3541.
[9] H. Schafer, G. Schneidereit, W.Z. Gerhardt, Anorg. Allg. Chem. 319 (1963) 372.
[10] J.P. Zheng, T.R. Jow, J. Electrochem. Soc. 142 (1995) L6.
[11] C.C. Hu, M.J. Liu, K.H. Chang, J. Power Sources 163 (2007) 1126.

[12] T.P. Gujar, V.R. Shinde, C.D. Lokhande, W.Y. Kim, K.D. Jung, O.S. Joo, Electrochem. Commun. 9 (2007) 504.
[13] K.H. Chang, C.C. Hu, Electrochem. Solid-State Lett. 7 (2004) A466.
[14] M. Min, K. Machida, J.H. Jang, K. Naoi, J. Electrochem. Soc. 153 (2006) A334.
[15] M. Wu, G.A. Snook, G.Z. Chen, D.J. Fray, Electrochem. Commun. 6 (2004) 499.
[16] Y.M. Zhou, X.Q. Xin, Chin. J. Inorg. Chem. 15 (1999) 273.
[17] C.F. Jin, X. Yuan, W.W. Ge, J.M. Hong, X.Q. Xin, Nanotechnology 14 (2003) 667.
[18] F. Li, L.Y. Chen, Z.O. Xu, J.M. Zhu, X.Q. Xin, Mater. Chem. Phys. 73 (2002) 335.
[19] T.Y. Zhou, Y.L. Song, J.M. Hong, X.Q. Xin, Nanotechnology 16 (2005) 536.
[20] F. Rouquerol, J. Rouquerol, K. Sing, Adsorption by Powers and Porous Solids: Principles Methodology and Applications, Academic Press, San Diego, 1999.
[21] J.P. Zheng, T.R. Jow, J. Power Sources 62 (1996) 155.
[22] A. Mckeown, P.L. Hagans, L.P.L. Carette, A.E. Eussell, K.E. Suider, D.R. Rolison, J. Phys. Chem. B 103 (1999) 4825.
[23] L. Cao, M. Lu, H.L. Li, J. Electrochem. Soc. 152 (2005) A871.
[24] J. Gamby, P.L. Taberna, P. Simon, J.F. Fauvarque, M. Chesneau, J. Power Sources 91 (2001) 109.
[25] Y.G. Wang, Z.D. Wang, Y.Y. Xia, Electrochim. Acta 50 (2005) 5641.
[26] Y.G. Wang, L. Cheng, Y.Y. Xia, J. Power Sources 153 (2006) 191.